Wavelength switching and scanning of the high-gain harmonic generation free-electron laser at the Dalian Coherent Light Source

Xinmeng Li, 1,2 Yong Yu, 3,* Qinming Li, 3 Siyue Liu, 1,4 Chong Wang, 1,3 Jiami Zhou, 1 Feiyang Yin, 1 Xu Shi, 1 Jitao Sun, 3 Jiahang Shao, 3 Xiaofan Wang, 3 Zhigang He, 1 Wenrui Dong, 1 Ling Jiang, 1 Jiayue Yang, 1,† Guorong Wu, 1 Weiqing Zhang, 1,‡ and Xueming Yang, 1 Paglian Coherent Light Source and State Key Laboratory of Chamical Reaction Dynamics

¹Dalian Coherent Light Source and State Key Laboratory of Chemical Reaction Dynamics, Dalian Institute of Chemical Physics, Chinese Academy of Sciences, Dalian 116023, China

²University of Chinese Academy of Sciences, Beijing 100049, China

³Institute of Advanced Light Source Facilities, Shenzhen 518107, China

⁴Key Laboratory of Materials Modification by Laser, Ion, and Electron Beams, Chinese Ministry of Education, School of Physics, Dalian University of Technology, Dalian 116024, China

(Received 13 June 2025; accepted 3 September 2025; published 9 October 2025)

The continuous wavelength tunability of free-electron lasers (FELs) offers significant potential for research across various scientific fields. The Dalian Coherent Light Source (DCLS), when operating in the high-gain harmonic generation (HGHG) mode, has demonstrated wavelength tuning capability within the vacuum ultraviolet (VUV) range of 50–150 nm. To address diverse experimental demands, it is imperative to have the capability of fast wavelength switching and scanning. This study presents three wavelength tuning strategies experimentally implemented at DCLS, each characterized by specific tuning ranges and resolutions: (i) full-range continuous wavelength switching over 50–150 nm, typically requiring more than 2 h; (ii) wide-range coarse wavelength scanning with approximately 20% variation within several minutes; and (iii) narrow-range fine wavelength scanning with a range of about 0.44% and a scanning resolution of 0.01% in less than 1 min. Each strategy has its own advantages and limitations, and their combination significantly enhances the flexibility of wavelength manipulation at DCLS, accommodating diverse user requirements.

DOI: 10.1103/2wmp-cb2b

I. INTRODUCTION

Free-electron lasers (FELs), characterized by their high power, narrow bandwidth, short pulse duration, and continuous wavelength tunability, have emerged as essential tools for advanced scientific research and offer significant potential for applications in fields such as energy science, chemistry, biology, materials science, and extreme ultraviolet lithography. At present, numerous high-gain FEL facilities have been proposed, are under construction, or have already been commissioned worldwide, such as Free-electron LASer in Hamburg (FLASH) [1] in Germany, Linac Coherent Light Source II (LCLS-II) [2] in the United States, Free Electron laser Radiation for Multidisciplinary

*Contact author: yuyong@mail.iasf.ac.cn †Contact author: yjy@dicp.ac.cn

[‡]Contact author: weigingzhang@dicp.ac.cn

Published by the American Physical Society under the terms of the Creative Commons Attribution 4.0 International license. Further distribution of this work must maintain attribution to the author(s) and the published article's title, journal citation, and DOI. Investigations (FERMI) [3] in Italy, European X-ray Free Electron Laser (European XFEL) [4] in Germany, Shanghai Soft X-ray Free Electron Laser (SXFEL) [5], Shanghai HIgh repetitioN rate XFEL and Extreme light facility (SHINE) [6], Shenzhen Superconducting Soft X-ray Free Electron Laser (S³FEL) [7], Dalian Advanced Light Source (DALS) [8], and Dalian Coherent Light Source (DCLS) [9.10] in China. These facilities cover a broad spectral range from the vacuum ultraviolet to hard x-rays and are all capable of continuous wavelength tuning. These facilities operate primarily in either the self-amplified spontaneous emission (SASE) mode [11,12] or seeding mode [13,14]. In the SASE mode, FEL radiation originates from electron beam shot noise, typically resulting in a broader bandwidth and reduced pulse stability. In contrast, seeding mode offers a narrower bandwidth but is significantly affected by the slice energy spread of the electron beam and is limited to harmonic conversion orders, restricting its extension into the hard x-ray regime.

Despite these inherent limitations, the continuously tunable wavelength characteristic of these FEL facilities remains a core advantage, significantly enhancing their potential for scientific applications, especially in the vacuum and extreme ultraviolet regions. For instance, wavelength scanning allows measurements of the photoionization efficiency (PIE) curve and resonance-enhanced multiphoton ionization spectra of radicals [15], thereby facilitating the detection of reactive intermediates in catalytic processes. Similarly, the reflectivity and transmissivity curves of material samples can be measured as functions of the FEL wavelength, to reveal their fundamental optical properties [16]. Additionally, fine wavelength scanning over a small range also enables accurate measurements of absorption edges, providing insights into the electronic structure and local coordination environments of the constituent atoms, thus supporting the design of advanced optical devices and novel materials [17,18]. Furthermore, molecular photochemistry can be studied by scanning the wavelength to measure molecular absorption spectra, clarifying photochemical reaction pathways relevant to fundamental research in atmospheric and interstellar chemistry [19,20]. Driven by these needs, extensive efforts have been made across FEL facilities to develop wavelength switching and scanning techniques. For example, Shanghai Deep Ultraviolet Free Electron Laser (SDUV-FEL) [21] can be continuously tuned from 350 to 800 nm by adjusting the undulator gap, seed laser wavelength, dispersive section strength, and beam trajectory. FERMI [22] has also conducted wide-range wavelength scanning across the 30-60 nm range by simultaneously adjusting the undulator gap, seed laser wavelength and power, time delay, and dispersive section strength. Meanwhile, the transmission measurements of Germanium were performed as a function of FEL wavelength. In addition, FERMI employed two distinct approaches to perform fine wavelength scanning within a narrow range. In the first method [22], the seed laser wavelength was incrementally changed by about 1 nm in total, with steps of approximately 0.1 nm, while the undulator gap was finely adjusted to satisfy the optimal resonance condition. Using this approach, the wavelength was scanned between 52.08 and 52.32 nm, during which the helium absorption edge was measured. The second approach [23] relies on adjusting the delay between the seed laser and the electron beam, thereby changing the beam lasing slice. Since the energy chirp differs along the beam, small-range wavelength scanning can be achieved. FLASH [24,25] has two undulator lines named FLASH1 and FLASH2. FLASH1 employs fixed-gap undulators, while FLASH2 operates with variable-gap undulators. Consequently, FLASH1 relies on adjusting the electron beam energy for wavelength tuning, while FLASH2 conducts wavelength tuning by adjusting the undulator gap. At Deep Ultra Violet FEL (DUV-FEL) [26,27] in Brookhaven National Laboratory (BNL), fine wavelength scanning is achieved by adjusting the radiofrequency (rf) phase and amplitude of the last accelerating structure, thereby modifying the beam energy chirp. As the phase is shifted from -45° to $+25^{\circ}$ relative to the crest phase, the wavelength changes from 263.4 to 266.1 nm, covering a tuning range of about 1%.

This article provides a comprehensive overview of the FEL wavelength tuning strategies at DCLS. Based on the HGHG mode, DCLS has been operating in the vacuum ultraviolet (VUV) region of 50–150 nm since its first lasing in 2016. As a user facility, it is expected to provide wavelength tuning capabilities to meet diverse experimental requirements regarding tuning range, efficiency, and resolution. To address these demands, three tuning methods have been implemented, including the full-range continuous wavelength switching, the wide-range coarse wavelength scanning, and the narrow-range fine wavelength scanning. The switching method covers the entire 50–150 nm range and is primarily employed for switching between user experiments or measurement systems that require large wavelength shifts. The wide-range coarse scanning and narrow-range fine scanning methods are primarily applied in user experiments requiring point-by-point scans within a limited wavelength range, enabling rapid scanning while maintaining stability in pulse energy and spectral characteristics. These three approaches collectively constitute the wavelength tuning strategy at DCLS and are described in detail as follows: Sec. II provides a comprehensive description of the DCLS facility, Secs. III–V present the principles and experimental results of the three wavelength tuning methods, and Sec. VI presents the conclusions.

II. DALIAN COHERENT LIGHT SOURCE

Dalian Coherent Light Source, with a total length of approximately 150 m, comprises three main sections: the electron linear accelerator (LINAC), the FEL amplifier, and the photon beamlines with experimental stations, as illustrated in Fig. 1. The electron beam is generated, accelerated, and compressed in the LINAC, ensuring that the beam energy, bunch length, and beam quality meet the stringent requirements for FEL lasing. The FEL amplifier mainly consists of modulator undulators (Mod), dispersion sections (DS), and radiator undulators, including planar permanent magnet undulators (PMUs) and elliptically polarized undulators (EPUs), to generate FEL pulses. At the end, the photon beamlines deliver the generated FEL pulses to the experimental stations for scientific research and simultaneously enable pulse diagnostics.

The LINAC contains two functional sections: an injector and a main accelerator. The injector primarily consists of a photocathode standing-wave electron gun [28] and a 3-mlong accelerating structure (A0). The copper cathode of the gun is illuminated by a drive laser, generating an electron beam with a bunch charge of 500 pC via the photoelectric effect [29]. The beam is accelerated to approximately 5 and 50 MeV at the exit of the gun and A0, respectively. The main accelerator consists of six S-band accelerating structures (A1–A6) operating at an rf frequency of 2.856 GHz, one X-band decelerating structure operating at 11.424 GHz, and a bunch compressor (BC) composed of four dipole magnets. The beam is accelerated off-crest with a positive rf phase in

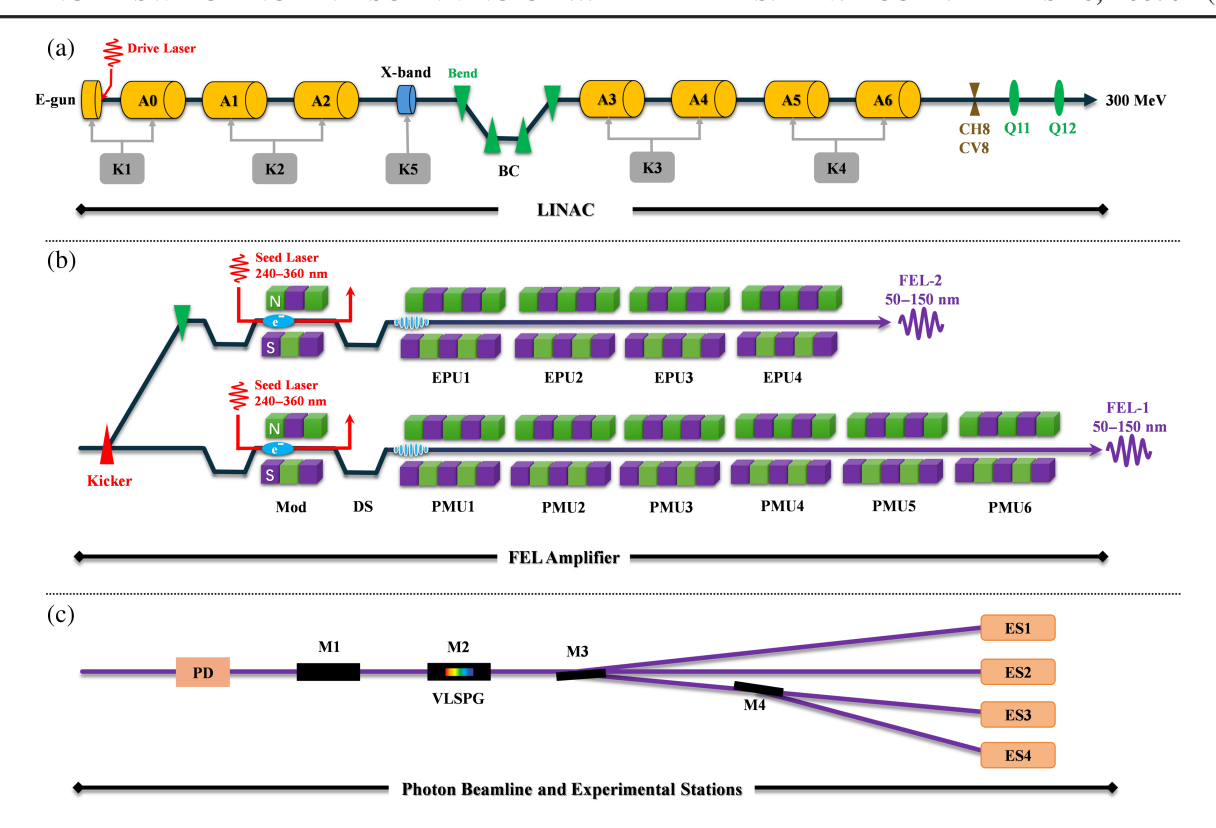


FIG. 1. Layout of Dalian Coherent Light Source. (a) Linear accelerator (LINAC), (b) FEL amplifier comprising FEL-1 and FEL-2 undulator lines, (c) photon beamline and experimental stations (ES).

A1 and A2 to introduce a positive energy chirp, and the bunch length is therefore compressed to about 0.6 ps after BC. Moreover, an X-band decelerating structure is employed at the entrance of the BC to linearize the beam energy chirp and achieve linear bunch compression, resulting in a flatter longitudinal phase space and a peak current of 300 A [30], thereby increasing the FEL pulse energy and narrowing the FEL bandwidth [31]. Afterward, the beam is accelerated offcrest with a negative rf phase in A3 and A4, thus providing a negative energy chirp to counteract the remaining positive one. Subsequently, the beam is boosted to 300 MeV in A5 and A6, which operate at the crest rf phase and are powered by a microwave klystron (K4). The electron beam parameters at the LINAC exit are listed in Table I.

As shown in Fig. 1(b), the beam switchyard distributes the electron beam into two undulator lines named FEL-1 and FEL-2 bunch by bunch with beam quality remaining essentially unchanged [32]. FEL-1 employs six PMUs [33] and thus can only generate linearly polarized radiation pulses in the horizontal direction, whereas FEL-2 uses four EPUs [34,35] that can produce pulses with variable polarization, such as linear, circular, and elliptical polarization. Both FEL lines operate in the HGHG mode, covering the VUV wavelength range of 50–150 nm with a pulse energy of 100 μJ and an FWHM pulse length of

TABLE I. Key parameters of DCLS.

Parameter	Value	Unit
Electron beam		
Energy	300	MeV
Energy spread	0.1	%
Bunch charge	500	рC
Peak current	300	A
Bunch length (RMS)	0.6	ps
Normalized emittance	1–2	mm-mrad
Repetition rate	20, Max: 50	Hz
Seed laser		
Wavelength	240-360	nm
Pulse duration (FWHM)	1	ps
Peak power	100	MW
Undulator (Mod/PMU/EPU)		
Period length	50/30/30	mm
Module length	1/3/3	m
FEL radiation		
Wavelength	50-150	nm
Pulse duration (FWHM)	~1	ps
Pulse energy	100	μJ
Polarization (FEL-1/2)	Linear/variable	
Tomization (TDD 1/2)	(linear to circular)	

1 ps. These parameters are also summarized in Table I. The FEL wavelength tuning in HGHG mode should simultaneously satisfy Eqs. (1) and (2) [36].

$$\lambda_{\text{FEL}} = \frac{\lambda_{\text{u}}}{2\gamma^2} \left(1 + \frac{K^2}{2} \right) \tag{1}$$

$$\lambda_{\text{FEL}} = \frac{\lambda_{\text{seed}}}{n} \tag{2}$$

Equation (1) defines the FEL resonance condition, where λ_{FEL} , γ , λ_{u} , and K represent the FEL wavelength, the relativistic Lorentz factor of the electron beam, the undulator period, and the undulator parameter, respectively. Equation (2) implies that the external seed laser wavelength λ_{seed} needs to be an integer multiple of the FEL wavelength, where n denotes the harmonic number.

Once the FEL pulses are produced, the photon beamlines deliver them to the experimental stations for scientific research and perform in situ diagnostics simultaneously. DCLS consists of two photon beamlines, both featuring nearly identical layouts, as depicted in Fig. 1(c). Each beamline comprises key optical components, including a toroidal mirror (M1) for focusing, a variable-line-spacing plane grating (VLSPG) spectrometer for online FEL spectral diagnostics [37], and several plane mirrors (M2/M3/M4) for precise FEL beam delivery to different experimental stations. Additionally, each beamline is equipped with a comprehensive suite of optical diagnostic devices, such as beamdefining apertures, intensity monitors, photodiodes, beam position monitors, and gas cells [38]. Among these, the PD and the VLSPG spectrometers are employed in our wavelength tuning experiments to measure the FEL pulse energy and diagnose the spectral characteristics, respectively.

III. FULL-RANGE CONTINUOUS WAVELENGTH SWITCHING

As a user facility, DCLS is designed to provide full-range wavelength tunability covering 50-150 nm to fulfill diverse experimental wavelength requirements. As illustrated in Fig. 1(b), the FEL-1 amplifier is composed of three segments, including a modulator (Mod) segment, a dispersive section (DS), and a radiator segment comprising 6 PMUs. In the modulator segment, the electron bunch and the seed laser pulse encounter and interact in a short undulator with a period length of 50 mm and a total length of 1 m, where the seed laser wavelength, as shown in Eq. (2), is set to an integer multiple n of the target FEL wavelength. According to Eq. (1), when the seed laser wavelength, the strength of the undulator, and the bunch energy satisfy the resonance condition, the seed laser imposes an energy modulation into the bunch. Subsequently, the energy-modulated bunch undergoes density modulation in the dispersive section, forming microbunching at intervals equal to the seed laser wavelength, resulting in a strong harmonic density component. Finally, the density-modulated bunch enters the radiator, and the PMU's gap is adjusted to satisfy the FEL lasing resonance condition in Eq. (1), thereby generating FEL pulses at the target harmonic wavelength.

To produce FEL pulses of 50–150 nm in HGHG mode, the external seed laser is designed to operate in a broad wavelength range of 240-360 nm. Due to the limited spectral coverage of a single crystal system, three distinct seed laser operation modes are employed at DCLS, corresponding to the wavelength bands of 240-267 nm, 265-300 nm, and 285-360 nm, as shown in Fig. 2(a). To provide a clear quantitative summary of the tuning capabilities enabled by these configurations, the FEL wavelength ranges accessible via the second to fifth harmonics for each mode are presented in Table II. The combination of these three seed laser modes enables continuous FEL tuning over the full 50-150 nm range through harmonic generation. In the 240–267 nm band, the 800 nm Ti: sapphire laser is first combined with the signal from the TOPAS optical parametric amplifier, and the resulting laser (SFS) from sum-frequency generation is subsequently subjected to second-harmonic generation (SHG), named the SHSFS scheme. For the 285-360 nm band, the signal output undergoes second-harmonic generation, and the resulting laser (SHS) is subjected to another SHG process, named the SHSHS scheme. In the intermediate 265-300 nm band, the idler from the TOPAS is combined with the 800-nm fundamental via sum-frequency generation, followed by SHG, named the SHSFI scheme. These tailored schemes enable flexible and efficient generation of ultraviolet seed pulses across the entire required wavelength range for HGHG operation.

To switch the FEL wavelength from 150 to 50 nm at DCLS, four main steps are required, as illustrated in Fig. 3. According to Table II, 150 nm corresponds to the second

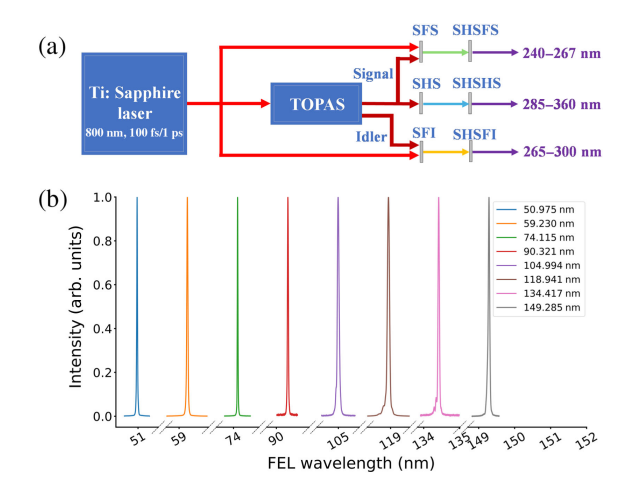


FIG. 2. Full-range continuous FEL wavelength switching at DCLS. (a) Three seed laser wavelength bands within the range of 240–360 nm. (b) Measured FEL spectra covering the full range of 50–150 nm, with intervals of about 15 nm.

	8				
Seed laser wavelength	Second harmonic	Third harmonic	Fourth harmonic	Fifth harmonic	Unit
240–267	120–133.5	80–89	60–66.75	50-53.4	nm
265-300	132.5-150	88.33-100	66.25-75	53-60	nm
285_360	142 5-150	95_120	71 25-90	57_72	nm

TABLE II. FEL wavelength coverage ranges under different seed laser modes and harmonic numbers at DCLS.

harmonic of 300 nm belonging to the SHSHS scheme or the SHSFI scheme, while 50 nm corresponds to the fifth harmonic of 250 nm belonging to the SHSFS scheme. The first step is to switch the seed laser to the 240-267 nm band. This process primarily involves replacing nonlinear crystals to enable a different frequency conversion scheme. Simultaneously, high-reflectivity mirror sets corresponding to the target seed laser wavelength band should be replaced. Based on prior operational experience, the delay line is coarsely adjusted to compensate for the optical path length difference between the two schemes. The second step is to adjust the seed laser wavelength to 250 nm so that it matches an integer multiple of the target FEL wavelength. Concurrently, the magnetic strengths of the modulator and radiator undulators are tuned according to Eq. (1), while keeping the electron beam energy constant. Since switching the seed laser mode in the first step alters characteristics such as peak power, arrival time, transverse position, and spot distribution of the seed laser, these variations affect its interaction with the electron bunch within the modulator. Therefore, in the third step, fine adjustments to the spatial overlap between the seed laser and the electron beam are made by observing their transverse distributions on the profile screens located upstream and downstream of the modulator. Additionally, the delay line is further optimized to improve its temporal synchronization. Finally, the large wavelength variation also induces distortions in the

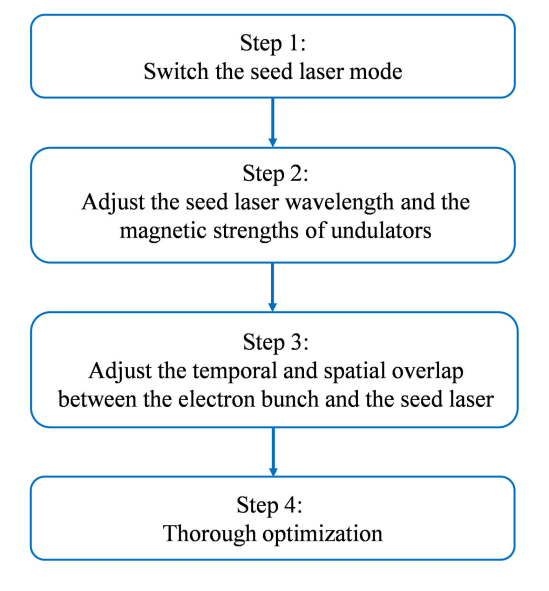


FIG. 3. Four main steps for full-range wavelength switching at DCLS.

transverse size and trajectory of the low-energy bunch, due to changes in the strong multipole magnetic fields of the undulators, which in turn degrade the FEL lasing performance. To compensate for these effects, a thorough optimization is required, including tuning the strength of the dispersion section, optimizing the lasing trajectory and transverse size of the bunch, and refining the temporal and spatial overlap between the electron bunch and the seed laser. After multiple rounds of optimization, saturated FEL output can be achieved. However, due to the coupling among these parameters, the overall optimization process is time consuming and typically takes more than 2 h.

Figure 2(b) shows the measured FEL spectra covering the full wavelength range of 50-150 nm with intervals of about 15 nm, where each spectrum at a certain FEL wavelength was measured by accumulating 200 consecutive FEL shots. This demonstrates the capability of fullrange continuous FEL wavelength switching at DCLS. Benefiting from the HGHG lasing mode, each spectrum exhibits a single spike and a near-Gaussian profile with a nearly Fourier-transform-limited bandwidth. These characteristics are summarized in Table III. At shorter wavelengths, higher harmonics shorten the FEL pulse duration, resulting in a broader spectral bandwidth. Additionally, chirp and phase noise in the seed laser further contribute to increasing the bandwidth [39,40]. These effects collectively cause the higher-order harmonic FEL pulses to deviate more from the Fourier transform limit.

IV. WIDE-RANGE COARSE WAVELENGTH SCANNING

Specific user experiments conducted at DCLS, such as the PIE curve-scanning experiments [41], need to record

TABLE III. Measured FEL spectral characteristics in the full-range continuous wavelength switching at DCLS.

Wavelength (nm)	FWHM bandwidth (nm)	Multiple of Fourier transform limit
50.975	0.022	5.82
59.230	0.035	6.71
74.115	0.020	2.48
90.321	0.031	2.53
104.994	0.055	3.37
118.941	0.067	3.18
134.417	0.043	1.61
149.285	0.045	1.37

the ionization signal with rapid wavelength scanning across broad spectral ranges. It takes minutes to scan within approximately $\pm 10\%$ of the center wavelength at DCLS.

Throughout the FEL wavelength tuning process, the FEL resonance condition defined in Eq. (1) should be satisfied [36]. It involves three variables, among which the undulator period λ_n is fixed. Therefore, FEL wavelength tuning can be achieved by adjusting the undulator parameter K, the electron beam energy E (i.e., the relativistic Lorentz factor γ), or both. The wavelength switching in the full-range method described in Sec. III was accomplished by adjusting multiple undulator strengths, whereas in the wide-range scanning, it was achieved more rapidly by varying only the beam energy via the K4 klystron, since the FEL photon energy range is just about one-tenth that of the former. Additionally, along with these adjustments, the beam size and trajectory should be controlled to obtain optimal FEL lasing performance. Unlike the full-range switching, which involves dozens of quadrupole and corrector magnets throughout the undulator line, the wide-range scanning relies on only two quadrupole magnets and two corrector magnets (Q11, Q12, CH8, and CV8, as shown in Fig. 1) located at the entrance of the FEL-1 undulator line to control the beam size and trajectory.

During the scanning, three principal aspects are considered. The first one is the seed laser wavelength accommodation according to Eq. (2), which supports only the same harmonic order in the scanning. The second one involves the electron beam energy adjustment mentioned above. Under a low-level rf closed-loop mode, the microwave amplitude and phase of the klystron K4 act as two independent variables; the beam energy can thus be adjusted by just regulating the K4 amplitude. The last one pertains to the beam transverse size and trajectory. Due to the relatively short undulator line (approximately 50 m), the transverse size and trajectory variations caused by the change in beam energy can be effectively controlled using the quadrupole magnets Q11 and Q12, along with the corrector magnets CH8 and CV8 in Fig. 1, respectively. Since DCLS operates in the VUV region with relatively long FEL wavelength lasing, the FEL pulse characteristics exhibit reduced sensitivity to the beam trajectory [42], so that only two corrector magnets, CH8 and CV8, are valid to control the beam trajectory in the DCLS wide-range wavelength scanning. Through this method, the number of optimized variables is reduced from dozens of parameters in the full-range switching to just 7, thereby reducing the manipulation complexity, shortening the wavelength tuning period to the order of minutes, and realizing the wavelength scanning.

Additionally, to evaluate the transverse beam size control, the beta function variations along the undulator line were theoretically simulated using the Methodical Accelerator Design (MAD) code [43]. According to the FEL resonance condition in Eq. (1), to change the FEL

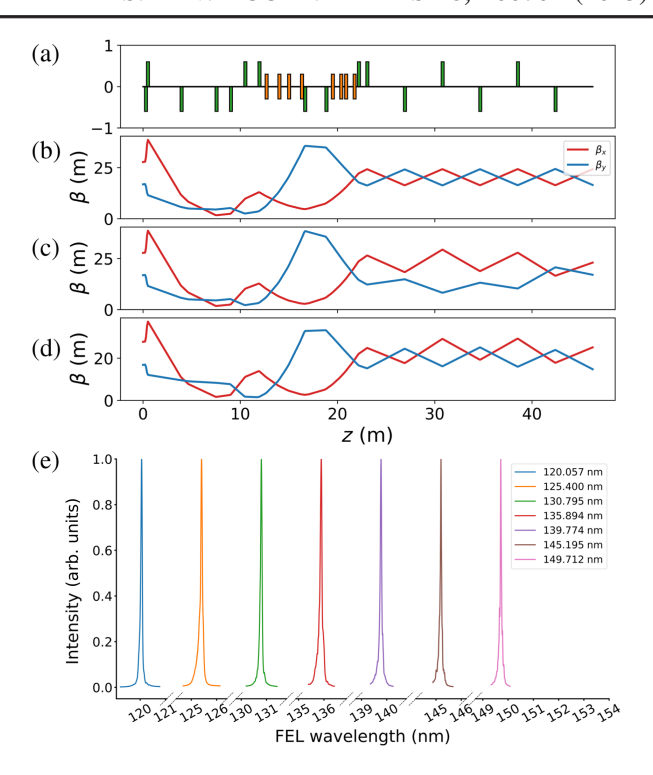


FIG. 4. Wide-range coarse FEL wavelength scanning at DCLS. (a) Magnet lattice of the FEL-1 undulator line starting from Q11 to Q12. (b) Beta functions at the nominal beam energy of 300 MeV. (c) Beta functions at the beam energy of 270 MeV with all magnet strengths unchanged. (d) Beta functions at the beam energy of 270 MeV with Q11 and Q12 optimized. (e) Measured FEL spectra from 120 to 150 nm with peak-to-peak FEL pulse energy variation within 4%.

lasing wavelength by 20%, the beam energy should be tuned by 10%, as expressed in Eq. (3).

$$\frac{\Delta \lambda_{\text{FEL}}}{\lambda_{\text{FEL}}} = -2 \frac{\Delta \gamma}{\gamma} \tag{3}$$

The nominal DCLS beam energy is 300 MeV, which implies that the required beam energy should be reduced to 270 MeV. The beta functions along the undulator line were evaluated under this change in beam energy, as shown in Fig. 4. Figure 4(a) illustrates the magnet lattice, where the green and orange blocks represent the quadrupole and dipole magnets, respectively. The quadrupole magnets Q11 and Q12, which are used to control the beam size, are located at the beginning of the lattice. The beta functions at the nominal beam energy of 300 MeV are shown in Fig. 4(b). They form a FODO cell in the undulator section (i.e., 23-46 m in the lattice), and their average values are $\beta_x = 20.30$ m and $\beta_{\rm v} = 20.27$ m. When decreasing the beam energy from 300 to 270 MeV and maintaining all magnet strengths unchanged, significant variations in the beta functions within the undulator section occur, as shown in Fig. 4(c). The resulting average horizontal beta function increases to

Wavelength (nm)	FWHM bandwidth (nm)	FEL pulse energy (μJ)	rms pulse energy jitter (%)
120.057	0.070	415.09	23.89
125.400	0.074	426.16	19.81
130.795	0.074	423.93	19.53
135.894	0.082	410.34	25.02
139.774	0.067	419.82	28.28
145.195	0.055	412.57	29.73
149.712	0.049	415.13	28.15

TABLE IV. Statistical parameters of the FEL spectra and corresponding pulse energies in the wide-range coarse FEL wavelength scanning at DCLS.

 $\beta_x = 22.60 \text{ m} (+11.33\%)$, while the vertical beta function decreases to $\beta_v = 13.62$ m (-32.81%). To restore the beta functions to their initial FODO configuration and thereby improve FEL radiation performance, the quadrupole magnets Q11 and Q12 were adjusted. The optimization was performed to minimize the relative change in the geometric mean of β_x and β_y with respect to their initial values, while also keeping their individual variations as small as possible. The corresponding results are shown in Fig. 4(d). Compared to the 300-MeV reference configuration, the vertical beta function β_v decreases from 20.27 to 20.08 m (-0.94%). Due to the limited sensitivity of Q11 and Q12 to the horizontal beta function, β_x increases from 20.30 to 23.01 m (+13.35%), leading to an estimated 5% reduction in the FEL saturation energy according to the Xie-Ming formula [44], which demonstrates that wavelength scanning within $\pm 10\%$ has a negligible impact on FEL lasing performance.

Following these configurations described above, a $\pm 10\%$ wide-range FEL wavelength scanning from 120 to 150 nm in 0.3-nm intervals was demonstrated at DCLS. Some of the spectra separated by about 5 nm are presented in Fig. 4(e). The corresponding spectral characteristic parameters and FEL pulse energies are detailed in Table IV. The key FEL lasing parameters remain almost unchanged during the entire scanning process; each spectrum maintains a single-spike, near-Gaussian profile with an FWHM bandwidth of about 0.07 nm. The corresponding FEL pulse energy at each wavelength, averaged over 600 pulses measured within 1 min, remains approximately 420 μJ. The rms jitter of the pulse energy at a fixed wavelength is approximately 25%, primarily resulting from fluctuations in the LINAC rf power and phase, variations in the energy, arrival time, and transverse position of the drive laser and seed laser, as well as magnetic field instabilities. The peak-to-peak FEL pulse energy variation, calculated from the maximum and minimum pulse energy values at approximately 100 wavelength points between 120 and 150 nm with 0.3-nm intervals, remained below 10%, demonstrating excellent stability during wavelength scanning.

As a practical application, the user experiments of PIE curve measurements were conducted by using the aforementioned wide-range wavelength scanning method. As shown in Fig. 5(a), the PIE curve of the neutral B₉ cluster

was measured with the wide-range scanned FEL pulses and a reflection time-of-flight mass spectrometer [41], which identified the first and second ionization potentials (IP1 and IP2) of the B_9 cluster at 8.45 ± 0.02 and 9.61 ± 0.02 eV, respectively. This work resolves the long-standing challenge in neutral boron clusters by demonstrating that the smallest three-dimensional structure of a boron cluster consists of nine boron atoms. In addition to the neutral boron cluster, the PIE curve of a Criegee intermediate CH_2OO was measured by using the same scanning and detection method in the wavelength range of 115-128 nm (9.7-10.8 eV). As shown in Fig. 5(b), the PIE curve obtained with the FEL pulses (red dots) clearly reveals a

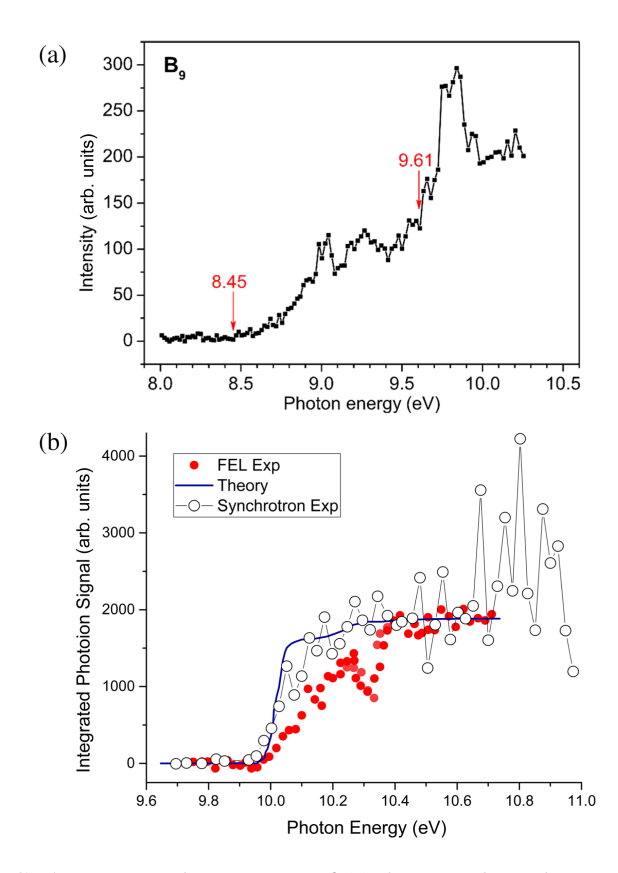


FIG. 5. Measured PIE curves of (a) the neutral B_9 cluster and (b) the Criegee intermediate CH_2OO obtained using the widerange coarse wavelength scanning method at DCLS.

sharp ionization onset near 10.0 eV, in good agreement with theoretical predictions (blue line) and previous synchrotron-based experiments (open circles) [45]. These results provide key experimental data for understanding the ionization dynamics of CH₂OO and further promote the study of its role in atmospheric chemistry. The differences between experimental results obtained using synchrotron radiation and DCLS can be attributed to two primary factors. First, the experimental conditions differ significantly: CH₂OO in the synchrotron experiment was sampled from a flow tube reactor, whereas in the DCLS experiment, CH₂OO was generated in a molecular beam undergoing supersonic expansion. This results in a substantially lower rotational temperature (~10 K) for CH₂OO in the DCLS experiment, which likely accounts for the additional spectroscopic structure observed between 10.3 10.4 eV in the PIE curves. Second, the higher pulse energy of the DCLS compared to synchrotron radiation leads to an improved signal-to-noise ratio, resulting in PIE curves with reduced fluctuations and enhanced spectral resolution. These findings demonstrate that DCLS offers significant advantages for trace species detection due to its high single-pulse energy, which enables measurements with superior signal-tonoise ratios compared to conventional synchrotron sources. This capability is particularly valuable for studying lowconcentration intermediates and obtaining high-quality spectroscopic data with minimal noise interference. These findings further demonstrate the versatility and broad applicability of the developed wide-range coarse wavelength scanning method for investigating a variety of molecular systems with diverse photon energy scanning requirements.

V. NARROW-RANGE FINE WAVELENGTH SCANNING

In addition to the full-range switching and wide-range scanning methods discussed above, specific user experiments require narrow-range but high-resolution wavelength scanning. For example, the absorption spectroscopy study of the water molecule near 124.0 nm demands scanning over a narrow range of approximately 0.2% with a fine scanning resolution [46].

In the HGHG mode, the FEL lasing wavelength is primarily determined by the microbunching period of the electron beam that is formed in the modulator segment and dispersion section. Normally, the FEL pulse is generated at the exact harmonic of the seed laser wavelength, as expressed in Eq. (2). However, a shift in the FEL wavelength occurs when the beam carries a linear energy chirp [23,31]. This effect was adopted at DCLS to achieve narrow-range fine wavelength scanning by precisely controlling the rf amplitude and phase of the K4 klystron to regulate the magnitude of linear energy chirp while keeping all other parameters unchanged. The principle of this fine wavelength scanning, based on simulations using an ideal electron beam, is illustrated in Fig. 6. The microbunching

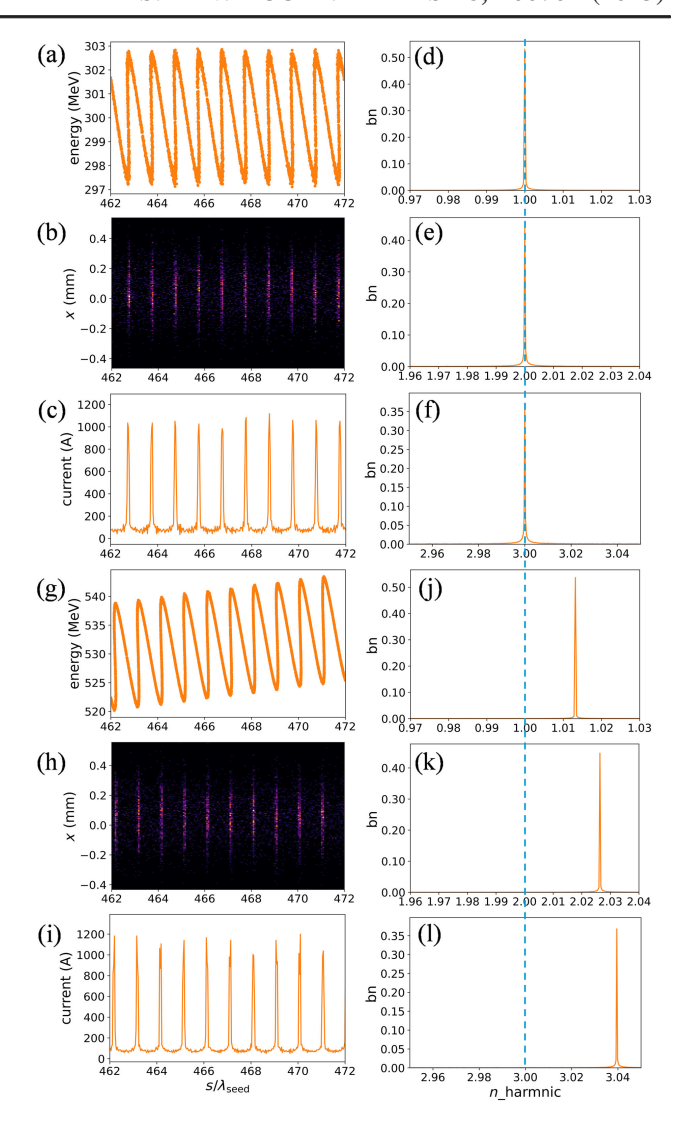


FIG. 6. Schematic diagrams of narrow-range fine FEL wavelength scanning, based on simulations using an ideal electron beam. (a)–(l) Distributions without energy chirp and with a linear energy chirp, respectively. (a),(g) Longitudinal phase space distributions of the electron beam at the exit of the dispersion section. (b), (h) Corresponding microbunching distributions. (c),(i) Corresponding current profiles, where s represents the longitudinal position inside the electron beam. (d)–(f) and (j)–(l) Bunching factor distributions for harmonic numbers n = 1-3, respectively.

period equals the seed laser wavelength when the electron beam operates without energy chirp, resulting in an FEL wavelength that strictly corresponds to the n th harmonic of the seed wavelength. When a linear energy chirp is applied, the microbunching period is scaled by a factor α , as determined in Eq. (4).

$$\alpha = 1 + kR_{56},\tag{4}$$

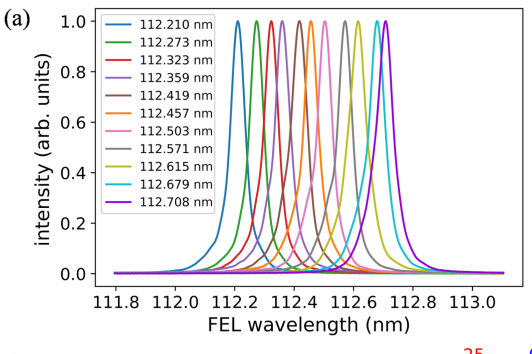
where k denotes the linear correlation coefficient between the energy chirp and the longitudinal position inside the beam, and $R_{56} < 0$ represents the momentum compaction factor of the dispersion section. If the beam carries a positive energy chirp (k > 0), i.e., the energy in the beam head is smaller than that in the tail, the microbunching period is compressed $(\alpha < 1)$, resulting in an increase in the corresponding harmonic number, as shown in Figs. 6(j)–6(l). As a result, a blue shift occurs in the FEL lasing wavelength. When the energy chirp is negative, this phenomenon is reversed, and a red shift in the FEL lasing wavelength emerges. Therefore, given the submillimeter scale R_{56} values typical of a dispersion section, precise control of the linear energy chirp enables narrow-range fine FEL wavelength scanning with a scanning resolution approaching or even below the FEL spectral bandwidth.

Precise energy chirp control was implemented by regulating the rf phase of klystron K4 at DCLS, imposing a quasilinear energy chirp on the electron beam. Meanwhile, the K4 rf amplitude was also accommodated accordingly to ensure that the beam energy satisfies the FEL resonance condition in Eq. (1), as variations in the rf phase would cause a deviation in beam energy. For electron beams with a linear energy chirp, the FEL wavelength variation rate is given by Eq. (4), where the linear correlation coefficient k is expressed in Eq. (5).

$$k = \frac{1}{E} \frac{\partial E}{\partial z} = \frac{2\pi}{\lambda_{\rm rf}} \frac{E_{\rm chirp} \sin \Delta \varphi_{\rm chirp}}{E_0 + E_{\rm chirp} \cos \Delta \varphi_{\rm chirp}},$$
 (5)

where $\lambda_{\rm rf}$ denotes the rf wavelength (0.105 m for the 2856 MHz rf frequency of K4), $E_{\rm chirp}$ is the crest accelerating energy of the K4 accelerating section, $\Delta \varphi_{\rm chirp}$ is the phase offset relative to the crest accelerating phase, and E_0 is the beam energy at the K4 entrance. As a result, the FEL lasing wavelength generated by an electron beam with a linear energy chirp can be expressed as Eq. (6).

$$\lambda_{\text{FEL}}^{\text{c}} = \left(1 + \frac{2\pi}{\lambda_{\text{rf}}} \frac{E_{\text{chirp}} \sin \Delta \varphi_{\text{chirp}} R_{56}}{E_0 + E_{\text{chirp}} \cos \Delta \varphi_{\text{chirp}}}\right) \frac{\lambda_{\text{seed}}}{n} \quad (6)$$



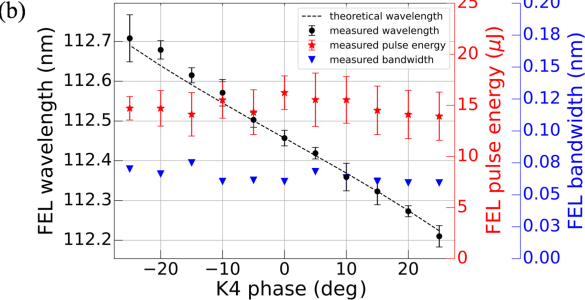


FIG. 7. Results of narrow-range fine FEL wavelength scanning at DCLS. (a) Measured FEL spectra during the scanning. (b) Relationship between the K4 phase and the corresponding FEL wavelength measured in the experiment (black dots with error bars) and calculated with theoretical formula Eq. (6) (black dashed curve), the measured FEL pulse energies (red stars with error bars), and the measured FWHM FEL spectral bandwidth (blue triangles).

Based on this theory, a fine wavelength scanning experiment at the third harmonic (n=3) was performed under a fixed seed laser wavelength of 337.3 nm at DCLS. The results are shown in Fig. 7 and Table V. In Fig. 7(a), the central orange spectrum corresponds to the case without electron beam energy chirp, while the left and right ones correspond to the cases with positive and negative energy chirps, respectively. The spectrum shapes remain nearly identical throughout the scanning, consistently exhibiting

TABLE V. Experimental conditions and results of the narrow-range fine FEL wavelength scanning at DCLS.

K4 phase (deg)	K4 amplitude (%)	Measured wavelength (nm)	FWHM bandwidth (nm)	FEL pulse energy (μJ)	rms pulse energy jitter (%)
25.0	90.5	112.210	0.059	13.94	16.93
20.0	87.5	112.273	0.059	14.11	16.73
15.0	85.5	112.323	0.060	14.51	16.40
10.0	84.7	112.359	0.063	15.54	14.67
5.0	84.0	112.419	0.068	15.55	16.78
0.0	84.5	112.457	0.060	16.24	10.16
-5.0	85.8	112.503	0.061	14.33	15.28
-10.0	87.0	112.571	0.060	15.53	11.46
-15.0	88.5	112.615	0.075	14.12	15.01
-20.0	92.0	112.679	0.066	14.71	11.83
-25.0	99.0	112.708	0.070	14.72	7.81

single-spike distributions with essentially unchanged bandwidth. Figure 7(b) shows the FEL spectral characteristics and the corresponding FEL pulse energy variation, along with the measured and theoretical dependence of the FEL wavelength on the K4 phase during the scanning. The black dashed curve represents the theoretical wavelength values calculated using Eq. (6) for different K4 phase offsets and amplitudes listed in Table V, while the black dots represent experimental data obtained under the respective K4 settings. The results demonstrate good agreement between the theoretical predictions and the experimental measurements. For each phase setting, 200 consecutive FEL spectra were recorded, and the standard deviation of the central wavelength was calculated as the error bars. The red stars show the FEL pulse energy variation during the scanning, and the error bars represent the rms jitter of the pulse energy. The blue triangles display the full width at half maximum (FWHM) bandwidth of the FEL spectra. The pulse energy, pulse energy jitter, and FWHM bandwidth remain stable throughout the scanning. These results are also summarized in Table V, with a scanning range of approximately 0.44% and a resolution of about 0.04%, which approaches the FEL bandwidth. Nevertheless, this narrow-range scanning method is theoretically capable of achieving an ultrafine resolution of 0.01% with a K4 phase variation of just 1°, while achieving wavelength tuning in less than 1 min enabled by its operational flexibility.

VI. DISCUSSION AND CONCLUSION

This study presents three HGHG-based FEL wavelength tuning methods with distinct operational ranges, all of which were experimentally implemented at DCLS to accommodate diverse user requirements. A summary of their respective performance is provided in Table VI. The full-range continuous switching method enables covering the entire operational range of DCLS (50–150 nm). However, this approach is complex and time-consuming as dozens of interdependent parameters need to be optimized, with a typical tuning period exceeding 2 h. The full-range switching method is primarily employed for large

wavelength shifts, such as when changing user experiments or measurement systems, typically occurring once every half month. However, for most experiments at DCLS, users generally request coarse scanning and fine scanning within a limited range, enabling rapid scanning while maintaining stability in pulse energy and spectral characteristics. The wide-range coarse wavelength scanning method affords tuning within $\pm 10\%$ of center wavelength in several minutes. This improvement is primarily attributed to the reduced number of regulated variables, including the wavelength and arrival time of the seed laser, the amplitude of klystron K4, and four magnetic field strengths. This method avoids optimizing six undulators and dozens of magnets, thereby significantly reducing optimization complexity and time required. Both methods typically achieve a relative wavelength tuning step of about 0.03%. The narrow-range scanning method is different in principle from the two above and features simpler operation. It operates by finely adjusting the electron beam energy chirp while maintaining a fixed seed laser wavelength, avoiding the need for adjusting the seed laser wavelength along with beam energy or undulator strength. At DCLS, the effective scanning resolution is constrained by the FEL spectral bandwidth, which is approximately 0.033%. When the scanning step becomes smaller than the FEL bandwidth, no distinguishable change will occur in the user's experimental outcome. Therefore, the experimental scanning resolution achieved was 0.04%, within a relative wavelength range of 0.44% and a typical scanning period of less than 1 min. Nevertheless, the narrow-range scanning method is theoretically capable of achieving a resolution of 0.01% with about 1° K4 phase variation, demonstrating its capability for high-resolution wavelength scanning.

Collectively, these three tuning methods provide DCLS with a comprehensive wavelength control capability, enabling it to meet the wavelength switching and scanning demands of diverse user experiments. Meanwhile, the scanning methods show significant potential for applications in various fields, such as materials science, energy catalysis, atmospheric science, and molecular photochemistry [47–50]. Furthermore, due to their advantages of fewer

TABLE VI. Summary of wavelength switching and scanning at DCLS.

Method	Wavelength range (nm)	Relative range (%)	Typical resolution (%)	Typical tuning variables	Typical number of variables	Typical tuning period
Full-range switching	50–150	100	0.03	Seed laser, undulators, magnets	Several dozen	More than 2 h
Wide-range scanning	120–150	22	0.03	Seed laser, beam energy, magnets	Seven	Several minutes
Narrow-range scanning	112.210–112.708	0.44	0.01	Energy chirp	Two	Less than 1 min

parameter adjustments, simplified optimization procedures, and rapid scanning capabilities, these methods could serve as a valuable reference for other HGHG-based FEL facilities.

ACKNOWLEDGMENTS

This work is supported by the National Natural Science Foundation of China (Grant No. 22288201), the Scientific Instrument Developing Project of Chinese Academy of Science (Grant No. GJJSTD20220001), DICP funding (Grant No. DICP I202304), the Strategic Priority Research Program of the Chinese Academy of Sciences (Grant No. XDB0970000, subject No. XDB0970100), and LiaoNing Revitalization Talents Program (Grant No. XLYC2202030). We would like to acknowledge Likai Wang (DICP) and Baoning Sun (DICP) for helpful discussions. We also thank the staff members of the Dalian Coherent Light Source [51] for providing technical support.

DATA AVAILABILITY

The data that support the findings of this article are not publicly available. The data are available from the authors upon reasonable request.

- [1] W. A. Ackermann *et al.*, Operation of a free-electron laser from the extreme ultraviolet to the water window, Nat. Photonics **1**, 336 (2007).
- [2] A. Brachmann, Commissioning of LCLS-II, in *Proceedings of the 32nd Linear Accelerator Conference*, LINAC-2024, Chicago, IL (JACoW, Geneva, Switzerland, 2024), p. 589.
- [3] E. Allaria *et al.*, Highly coherent and stable pulses from the FERMI seeded free-electron laser in the extreme ultraviolet, Nat. Photonics **6**, 699 (2012).
- [4] W. Decking et al., A MHz-repetition-rate hard x-ray freeelectron laser driven by a superconducting linear accelerator, Nat. Photonics 14, 391 (2020).
- [5] B. Liu *et al.*, The SXFEL upgrade: From test facility to user facility, Appl. Sci. 12, 176 (2022).
- [6] Z. T. Zhao, H. Ding, and B. Liu, Shanghai Hard X-Ray FEL facility progress status, in *Proceedings of the 15th International Particle Accelerator Conference, IPAC-2024, Nashville, TN* (JACoW, Geneva, Switzerland, 2024), p. 967.
- [7] X. Wang et al., Physical design for Shenzhen Superconducting Soft X-Ray Free-Electron Laser (S³FEL), in Proceedings of the 14th International Particle Accelerator Conference, Venice, Italy (JACoW, Geneva, Switzerland, 2023), p. 1852.
- [8] X. Li et al., An injector testbed based on a direct current gun and an interchangeable very high frequency gun for superconducting continuous-wave free-electron lasers, J. Synchrotron Radiat. 32, 838 (2025).

- [9] Y. Yu et al., Dalian extreme ultraviolet coherent light source, Chin. J. Lasers (Chin. Ed.) (1983–) 46, 0100005 (2019).
- [10] J. Sun, X. Li, J. Yang, L. Zeng, J. Shao, Y. Yu, W. Zhang, and X. Yang, An experimental application of machine learning algorithms to optimize the FEL lasing via beam trajectory tuning at Dalian Coherent Light Source, Nucl. Instrum. Methods Phys. Res., Sect. A 1063, 169320 (2024).
- [11] A. M. Kondratenko and E. L. Saldin, Generating of coherent radiation by a relativistic electron beam in an ondulator, Part. Accel. 10, 207 (1980), https://scispace.com/papers/generating-of-coherent-radiation-by-a-relativistic-electron-2dvmlgxc2w.
- [12] R. Bonifacio, P. Pierini, C. Pellegrini, J. Rosenzweig, and G. Travish, Slippage, noise and superradiant effects in the UCLA FEL experiment, Nucl. Instrum. Methods Phys. Res., Sect. A **341**, 285 (1994).
- [13] L. H. Yu, Generation of intense UV radiation by subharmonically seeded single-pass free-electron lasers, Phys. Rev. A 44, 5178 (1991).
- [14] L. H. Yu et al., First ultraviolet high-gain harmonic-generation free-electron laser, Phys. Rev. Lett. 91, 074801 (2003).
- [15] J. Quan *et al.*, A free electron laser-based 1 + 1' resonance-enhanced multiphoton ionization scheme for rotationally resolved detection of OH radicals with correct relative intensities, J. Mol. Spectrosc. **380**, 111509 (2021).
- [16] F. Bencivenga *et al.*, Reflectivity enhancement in titanium by ultrafast XUV irradiation, Sci. Rep. 4, 4952 (2014).
- [17] F. Bencivenga, F. Capotondi, E. Principi, M. Kiskinova, and C. Masciovecchio, Coherent and transient states studied with extreme ultraviolet and x-ray free electron lasers: Present and future prospects, Adv. Phys. **63**, 327 (2014).
- [18] M. Malvestuto, R. Ciprian, A. Caretta, B. Casarin, and F. Parmigiani, Ultrafast magnetodynamics with free-electron lasers, J. Phys. Condens. Matter **30**, 053002 (2018).
- [19] Y. Zhao et al., Rotational and nuclear-spin level dependent photodissociation dynamics of H₂S, Nat. Commun. 12, 4459 (2021).
- [20] Y. Wu *et al.*, Photodissociation dynamics of SO₂ via the G1B1 state: The O(1D2) and O(1S0) product channels, J. Chem. Phys. **160** (2024).
- [21] B. Liu *et al.*, Demonstration of a widely-tunable and fully-coherent high-gain harmonic-generation free-electron laser, Phys. Rev. ST Accel. Beams **16**, 020704 (2013).
- [22] E. Allaria *et al.*, Tunability experiments at the FERMI@E-lettra free-electron laser, New J. Phys. **14**, 113009 (2012).
- [23] F. Sottocorona *et al.*, Wavelength control in high-gain harmonic generation seeded free-electron lasers, Phys. Rev. Accel. Beams **26**, 090702 (2023).
- [24] B. Faatz *et al.*, Simultaneous operation of two soft x-ray free-electron lasers driven by one linear accelerator, New J. Phys. **18**, 062002 (2016).
- [25] B. Faatz *et al.*, The FLASH facility: Advanced options for FLASH2 and future perspectives, Appl. Sci. **7**, 1114 (2017).
- [26] T. Shaftan *et al.*, Experimental demonstration of wavelength tuning in high-gain harmonic generation free electron laser, in *Proceedings of the 26th International*

- Free Electron Laser Conference, Trieste, Italy (JACoW, Geneva, Switzerland, 2004), p. 282.
- [27] T. Shaftan and L. H. Yu, High-gain harmonic generation free-electron laser with variable wavelength, Phys. Rev. E 71, 046501 (2005).
- [28] L. Zheng et al., Development of S-band photocathode RF guns at Tsinghua University, Nucl. Instrum. Methods Phys. Res., Sect. A 834, 98 (2016).
- [29] A. Einstein, Concerning an heuristic point of view toward the emission and transformation of light, Am. J. Phys. 33, 367 (1965).
- [30] Y. Yu *et al.*, The X-band linear compression system in Dalian Coherent Light Source, in *Proceedings of the 39th Free Electron Laser Conference, FEL2019, Hamburg, Germany* (JACoW, Geneva, Switzerland, 2019), p. 625.
- [31] G. Wang, C. Feng, H. Deng, T. Zhang, and D. Wang, Beam energy chirp effects in seeded free-electron lasers, Nucl. Instrum. Methods Phys. Res., Sect. A **753**, 56 (2014).
- [32] V. Balandin, W. Decking, and N. Golubeva, Optics for the beam switchyard at the European XFEL, in *Proceedings of* the 2nd International Particle Accelerator Conference, IPAC-2011, San Sebastián, Spain (EPS-AG, Spain, 2011), pp. 2016.
- [33] K. Halbach, Permanent magnet undulators, J. Phys. (Paris), Colloq. 44, C1-211 (1983).
- [34] C. Hwang and S. Yeh, Various polarization features of a variably polarized undulator with different phasing modes, Nucl. Instrum. Methods Phys. Res., Sect. A 420, 29 (1999).
- [35] M. Weiss et al., The elliptically polarized undulator beamlines at BESSY II, Nucl. Instrum. Methods Phys. Res., Sect. A 467–468, 449 (2001).
- [36] P. Schmüser, M. Dohlus, and J. Rossbach, Ultraviolet and Soft X-ray Free-Electron Lasers: Introduction to Physical Principles, Experimental Results, Technological Challenges (Springer, New York, 2008), Vol. 229.
- [37] C. Li, S. Wei, X. Du, L. Du, Q. Wang, W. Zhang, G. Wu, D. Dai, and X. Yang, On-line spectral diagnostic system for Dalian Coherent Light Source, Nucl. Instrum. Methods Phys. Res., Sect. A 783, 65 (2015).
- [38] M. Wang, Y. Yu, J. Yang, Q. Li, and W. Zhang, Multifunctional gas cell in the vacuum ultraviolet free-electron laser beamline, Rev. Sci. Instrum. **95**, 063101 (2024).
- [39] E. Allaria, M. B. Danailov, W. M. Fawley, L. Giannessi, and E. Ferrari, Measurements of the FEL-bandwidth scaling with harmonic number in a HGHG FEL, in

- Proceedings of the 36th International Free Electron Laser Conference, FEL2014, Basel, Switzerland (JACoW, Geneva, Switzerland, 2014), p. 227.
- [40] D. Ratner, A. Fry, G. Stupakov, and W. White, Laser phase errors in seeded free electron lasers, Phys. Rev. ST Accel. Beams **15**, 030702 (2012).
- [41] C.-Q. Xu et al., Observation of the smallest threedimensional neutral boron cluster, Angew. Chem., Int. Ed. 64, e202419089 (2025).
- [42] Z. Huang and K.-J. Kim, Review of x-ray free-electron laser theory, Phys. Rev. ST Accel. Beams 10, 034801 (2007).
- [43] H. Grote and F. C. Iselin, The MAD program (methodical accelerator design): Version 8.10; user's reference manual, Report No. CERN-SL-90-13-AP-Rev-3, CERN, Geneva, 1993.
- [44] X. Ming, Design optimization for an x-ray free electron laser driven by SLAC linac, in *Proceedings of the Particle Accelerator Conference, Dallas, TX, 1995* (IEEE, New York, 1995), pp. 183.
- [45] O. Welz, J. D. Savee, D. L. Osborn, S. S. Vasu, C. J. Percival, D. E. Shallcross, and C. A. Taatjes, Direct kinetic measurements of Criegee intermediate (CH₂OO) formed by reaction of CH₂I with O₂, Science **335**, 204 (2012).
- [46] K. Yuan, Y. Cheng, L. Cheng, Q. Guo, D. Dai, X. Wang, X. Yang, and R. N. Dixon, Nonadiabatic dissociation dynamics in H₂O: Competition between rotationally and non-rotationally mediated pathways, Proc. Natl. Acad. Sci. U.S.A. 105, 19148 (2008).
- [47] F. Bridou, M. Cuniot-Ponsard, and J.-M. Desvignes, Experimental determination of optical constants in the vacuum ultra violet wavelength region between 80 and 140 nm: A reflectance versus thickness method and its application to ZnSe, Opt. Commun. **271**, 353 (2007).
- [48] Y. Chang, M. N. R. Ashfold, K. Yuan, and X. Yang, Exploring the vacuum ultraviolet photochemistry of astrochemically important triatomic molecules, Natl. Sci. Rev. 10, nwad158 (2023).
- [49] Y. Chang *et al.*, Tunable VUV photochemistry using vacuum ultraviolet free electron laser combined with H-atom Rydberg tagging time-of-flight spectroscopy, Rev. Sci. Instrum. **89**, 063113 (2018).
- [50] L. C. Lee and M. Suto, Quantitative photoabsorption and fluorescence study of H₂O and D₂O at 50–190 nm, Chem. Phys. 110, 161 (1986).
- [51] https://cstr.cn/31127.02.DCLS